

Cite this: *Energy Environ. Sci.*, 2012, **5**, 8716

www.rsc.org/ees

PAPER

PbTe–PbSnS₂ thermoelectric composites: low lattice thermal conductivity from large microstructures†Steven N. Girard,^a Thomas C. Chasapis,^{ab} Jiaqing He,^{ac} Xiaoyuan Zhou,^d Euripides Hatzikraniotis,^b Ctirad Uher,^d Konstantinos M. Paraskevopoulos,^b Vinayak P. Dravid^c and Mercouri G. Kanatzidis^{*a}

Received 9th June 2012, Accepted 24th July 2012

DOI: 10.1039/c2ee22495j

Recent advances in the field of thermoelectrics have shown embedding appropriate nanostructures can significantly suppress the lattice thermal conductivity and therefore enhance ZT . Here we report a new class of thermoelectric composites of PbTe–PbSnS₂. PbSnS₂ is a naturally layered material (space group $Pnma$) comprised of Sn–Pb bilayers approximately 0.6 nm in thickness. High resolution transmission electron microscopy reveals the PbSnS₂ segregates into coherent lamellar structures 50–100 nm in thickness that extend 100 nm to 15 μ m in length. Despite the relatively large size of the PbSnS₂ precipitates, we find that incorporation of PbSnS₂ in PbTe results in significant reduction in lattice thermal conductivity to 0.4–0.65 W m^{−1} K^{−1} over the temperature range 300–700 K, a reduction of 50–70% over bulk PbTe. As a result, a maximum ZT of 1.1 is obtained for ingot samples of the PbTe–PbSnS₂ 6% composition. We provide extensive characterization of the physical, structural, and chemical properties of this materials system including powder X-ray diffraction, infrared reflectivity, scanning and transmission electron microscopy, and thermoelectric properties measurements. The synthesis method is simple and general, opening possibilities for similar systems to yield materials exhibiting low lattice thermal conductivity without it being necessary to embed nanoscale (5–20 nm) features.

^aDepartment of Chemistry, Northwestern University, Evanston, IL 60208, USA. E-mail: m-kanatzidis@northwestern.edu

^bPhysics Department, Aristotle University of Thessaloniki, GR-54124, Thessaloniki, Greece

^cDepartment of Materials Science and Engineering, Northwestern University, Evanston, IL 60208, USA

^dDepartment of Physics, University of Michigan, Ann Arbor, MI 48109, USA

† Electronic supplementary information (ESI) available: Details of the Kramers–Kronig transformation, thermal diffusivity, density, specific heat, and Hall coefficient of samples used in this study. See DOI: 10.1039/c2ee22495j

Introduction

Thermoelectric heat-to-power generation is a physical process exhibited in materials, and was first observed by Thomas Seebeck in 1821.^{1,2} The overall performance of thermoelectric materials is determined by the thermoelectric figure of merit ZT , which is defined as $ZT = (S^2 \sigma T / \kappa)$, where T is operating temperature, σ is electrical conductivity, and κ is thermal conductivity (a sum of the electronic κ_{elec} and lattice κ_{lat} vibrations). In practice, any heat-generating process (such as the combustion of fossil fuels in

Broader context

The significance and scale of the energy challenges facing the world necessitate consideration of all options for renewable power generation. Thermoelectric materials, which directly convert heat into electricity, are particularly promising in this regard: heat-producing processes, such as the combustion of fossil fuel in power plants or commercial vehicles, may become more efficient if wasted heat may be recouped as electricity. To realize this goal, researchers have been focusing on improving the efficiencies of thermoelectrics by reducing the lattice thermal conductivity of existing thermoelectric materials through nanostructuring. By incorporating nanostructures below the mean free path of phonons, generally less than 20 nm, increased phonon scattering aids to increase thermoelectric figure of merit. However, in some thermoelectric systems embedding nanostructures may be difficult. Here we report low lattice thermal conductivity in PbTe–PbSnS₂ composites. PbSnS₂ forms a stable pseudo-binary within PbTe, producing microstructures between 100 nm to 15 μ m. Despite the relatively large PbSnS₂ microstructures, we observe low values of lattice thermal conductivity comparable with many nanostructured PbTe systems, providing an alternative route toward thermoelectric materials with low lattice thermal conductivity.

cars and power plants) can be made more efficient by recouping lost waste heat. An unfortunate reality of conventional thermoelectric materials is that the electronic and thermal transport are coupled, and are therefore difficult to control independently. Because of this, the highest ZT for conventional bulk materials (Bi_2Te_3 , PbTe , and SiGe) is between 0.8 and 1, corresponding to a 5–10% efficiency given a cold side of room temperature and a temperature differential of 350 K.³ To make thermoelectric materials economically viable for wide-scale use, the ZT must be increased. To accomplish this, nanostructured thermoelectrics possess intriguing possibilities to increase thermoelectric efficiency and utility of thermal-to-electrical power generation.^{4–6} Nanostructuring in bulk materials was discovered first in the $\text{AgPb}_m\text{SbTe}_{2+m}$ (LAST, n-type) and $\text{AgPb}_m\text{SbTe}_{2+m}$ (SALT, p-type) systems with nanostructure length scales on the order of 2–50 nm.^{7,8}

Recently, impressive increases in ZT have been reported in a variety of nanostructured forms of thermoelectric materials, including nanoparticle assemblies and nanowires,^{9–12} pressed nanopowders,^{13–16} and nanostructured bulk materials.^{7,17} A growing consensus within the community shows that nanostructures can effectively scatter phonons and therefore reduce lattice thermal conductivity κ_{lat} . Due to the disparity in mean free paths and wavelengths of electrons and phonons, proper nanostructures do not significantly scatter electrons and therefore do not alter electronic transport ($S^2\sigma$), resulting in increased ZT .^{5,18–21}

The nanostructured thermoelectric material $\text{Pb}_{0.95}\text{Sn}_{0.05}\text{Te}$ – PbS 8% has been demonstrated as having an enhanced ZT as a direct result of naturally formed nanostructures.²² For the nominal $\text{PbS}_{1-x}\text{Te}_x$ system, spinodal decomposition (where $x = 0.3$)²³ and nucleation and growth (where $x = 0.08$)²⁴ phase transformations naturally phase separate PbS nanocrystals that beneficially reduce lattice thermal conductivity. The incorporation of ~5% SnS into the PbTe matrix resulted in more robust samples for properties measurements and characterization, and appeared similar to the PbTe – PbS system. Conversely, $\text{Pb}_{1-x}\text{Sn}_x\text{Te}$ is a known solid solution. SnTe is naturally p-type owing to Sn vacancies, which alloys sufficiently Sn -rich $\text{Pb}_{1-x}\text{Sn}_x\text{Te}$ alloys to be interesting p-type thermoelectric materials.²⁵

Herein we show by combining the PbTe – SnTe – PbS thermoelectric systems, we produce a completely new composite of PbTe – PbSnS_2 . The formation of a distinct and independent PbSnS_2 phase occurs at increased concentrations (>5%) of Sn into PbTe – PbS . PbSnS_2 is the known mineral tellite and has a layered structure of approximately 0.6 nm in width. In contrast to the PbTe – PbS system, PbTe – PbSnS_2 appears to phase separate by a eutectoid-like transformation which results in large PbSnS_2 lamellae, *i.e.* >50 nm. We show here that PbTe – PbSnS_2 composites exhibit low lattice thermal conductivity despite having microstructures well above the mean free path of phonons; we attribute the low lattice thermal conductivity to the naturally confined bilayers of PbSnS_2 . It has been shown that there exists a high degree of coherency between PbSnS_2 and cubic PbS ;²⁶ we show in this work that semicoherent interfaces are observed at the PbSnS_2 – PbTe interfaces. The corresponding lattice thermal conductivity is significantly reduced over bulk PbTe , enhancing the ZT .

Experimental

Synthesis

Stock PbTe , SnTe , and PbS materials were synthesized using high-purity Pb (99.99%, American Elements), Te (99.999%, 5 N Plus), S (99.99%, 5 N Plus) and Sn (99.999%, Atlantic Metals) by flame-sealing the starting elements into fused silica ampoules under a residual pressure of $\sim 10^{-4}$ Torr and reacting at least 50 °C above the melting point in high-temperature furnaces. PbTe – PbSnS_2 was synthesized by stoichiometric addition of appropriate quantities of PbTe , SnTe , and PbS using the same method. Certain samples were doped with 0.055 mol% PbI_2 n-type dopant (99.999%, Aldrich). For example, synthesis of ~8 g PbTe – PbSnS_2 6% + 0.055% PbI_2 would require 6.7932 g PbTe , 0.3657 g SnTe , 0.7105 g PbS , and 0.0063 g PbI_2 . All samples were held at 1050 °C for approximately 8 h, inverted several times at the melt to ensure complete mixing, and quenched from the melt. The resulting ingots were sectioned using a circular wire saw and polished using a Buehler Isomet grinder/polisher.

Powder and single crystal X-ray diffraction

Finely ground samples were placed in an Inel CPS-120 X-ray powder diffractometer using Ni-filtered Cu K_α radiation ($\lambda = 1.54056$ Å) in reflection geometry, equipped with a position sensitive detector and operating at 40 kV and 20 mA.

Electrical conductivity/Seebeck coefficient measurements

Electrical conductivity and Seebeck coefficient (or thermopower) were measured on polished parallelepipeds approximately $2 \times 2 \times 8$ mm in an ULVAC ZEM-3 electrical conductivity and Seebeck coefficient system. Samples were sandwiched between two Ni electrodes with two probe thermocouples providing forced contacts on one side. The sample chamber was evacuated and back-filled with approximately 0.1 atm He, and heated from room temperature to 400 °C using an IR furnace. Electrical conductivity is measured using standard 4-point probe technique.²⁷ The Seebeck coefficient is calculated by measuring average induced voltage resulting from temperature gradients of 5, 10, and 15 K provided by resistive Pt coils located beneath one electrode.

IR reflectivity measurements

Infrared (IR) reflectivity measurements were performed on finely polished PbTe – PbSnS_2 samples using a Bruker 113V FTIR spectrometer with a resolution of about 2 cm^{-1} , at nearly normal incidence, in the 100–1500 cm^{-1} spectral region, at room temperature. The reflection coefficient was determined by typical sample-in-sample-out method with a mirror as the reference. The obtained experimental reflectivity spectrum $R(\omega)$ (*e.g.*, the response of the material to the incident electromagnetic radiation) may be characterized by a complex dielectric function (complex permittivity). The complex dielectric function $\epsilon(\omega)$ is related to the measured reflectivity *via* the relation:

$$R(\omega) = \left(\frac{\sqrt{\varepsilon(\omega)} - 1}{\sqrt{\varepsilon(\omega)} + 1} \right)^2 \quad (1)$$

The experimental reflectivity spectrum was analyzed by the Kramers–Kronig (KK) transformation technique to obtain the real and imaginary parts of the complex dielectric function (see ESI for details†). In general, the imaginary part of the dielectric function is related to the dissipation or loss of energy within the material. The frequencies where absorption by the longitudinal vibrations occurs, *i.e.* the free carrier oscillations, appear as peaks in the computed Kramers–Kronig $\text{Im}(-1/\varepsilon)$ spectrum.

Hall measurements

High temperature Hall effect measurements were carried out by an in-house high temperature/high magnetic field Hall apparatus. It consists of a nine Tesla air-bore superconducting magnet with a water-cooled oven inside the bore of the magnet, and a Linear Research AC bridge with 16 Hz excitation. Four-wire AC Hall measurements are performed on parallelepiped samples with the typical size of $1.5 \times 3 \times 10$ mm to temperatures of 850 K under argon atmosphere.

Thermal conductivity

Thermal diffusivity and specific heat of samples were measured on a Netzsch LFA 457. Coins measuring approximately 8 mm in diameter by 2 mm in thickness were heated from room temperature to 400 °C (~700 K). Total thermal conductivity was calculated using the equation $\kappa_{\text{tot}} = \alpha C_p d$, where κ_{tot} is total thermal conductivity, α is thermal diffusivity, C_p is specific heat, and d is density. Density was calculated from the sample dimensions and mass, and C_p was calculated relative a Pyroceram 9606 reference. The electronic contribution to total thermal conductivity κ_{elec} was calculated using the Wiedemann–Franz law, $\kappa_{\text{elec}} = \sigma T L$ (where σ = electrical conductivity, T = temperature, and L is the calculated Lorenz number). The lattice component κ_{lat} is then calculated using the relation $\kappa_{\text{lat}} = \kappa_{\text{tot}} - \kappa_{\text{elec}}$.

Scanning electron microscopy (SEM)

The microstructure of finely polished sample surfaces were observed and identified using a Hitachi S3400 SEM equipped with a back-scattered electron (BSE) detector operating at 20 kV voltage and 15 μA current at a working distance of 10 mm. Differences in phase composition were successfully identified using energy dispersive X-ray spectroscopy (EDS) analysis using the program Inca.

High-resolution images were observed using a FEI Helios Nanolab FIB/SEM. Imaging using the electron beam was accomplished at 5 kV voltage with a 98 pA current, while milling using the ion beam was accomplished at 30 kV voltage with 2.8 nA current. Areas of the sample were bombarded with Ga^+ ions, resulting in preferential etching of the sample along grain boundaries and differing phases. The resulting image provides a more clear representation of the microstructure, with minimized appearance of surface defects and scratches.

Transmission electron microscopy (TEM)

Samples were thinned to electron-transparent foils using both a conventional polishing method as well as through preparation in the FIB/SEM. Images were obtained using a JEOL 2100F (field emission TEM) operating at 200 kV using a double-tilt holder.

Results and discussion

Solid state chemistry and powder X-Ray diffraction

In a previous study of the PbTe–PbS system, it was found that substituting ~5 at.% SnS for PbTe could generate better quality polycrystalline ingots with good cutting and polishing properties.²² Here, we extend that work and present a more systematic study of Sn substitution on the Pb sites of PbTe within PbTe–PbS. We prepared samples of $(\text{Pb}_{1-x}\text{Sn}_x\text{Te})_{0.7}(\text{PbS})_{0.3}$ where $x = 0, 0.01, 0.05, 0.1, 0.2$, and 0.5 to better understand the phases formed for PbTe–PbS 30% with increasing Sn substitution. We specifically chose the 30% PbS concentration for two reasons: (1) at larger concentrations, the characteristic Bragg reflections of PbS are observable by powder X-ray diffraction (PXRD) when added to PbTe, and (2) a large volume density of PbS precipitates may be easily observed by conventional SEM/TEM techniques. We have shown previously that for samples of PbTe–PbS 30% quenched directly from the melt, there is no observable phase separation of PbS from PbTe, as evidenced by PXRD and high resolution TEM.²³ Here, PXRD analysis revealed that the addition of even 1% SnS to PbTe–PbS 30% (*i.e.* a composition of $\text{Pb}_{0.99}\text{Sn}_{0.01}\text{Te}$ –PbS 30%) for rapidly quenched samples results in an observable amount of the minor PbS, Fig. 1a. As Sn is increasingly substituted for Pb, an increase in intensity of the (111) and (200) PbS reflections suggest increased concentration of the PbS second phase, and therefore increased immiscibility between PbTe and PbS. Concurrently, a noticeable shoulder on the (200) peak of PbTe is observed with Sn substitution, which grows to a clearly defined reflection at 10% Sn substitution, Fig. 1b. This suggests the coexistence of two matrix phases at this composition: one that is relatively pure PbTe, the other a solid solution between PbTe and PbS.

As Sn is substituted at concentrations greater than 10%, a new phase of PbSnS_2 is observed, which is preferentially formed (relative to PbS) at concentrations above 20%, Fig. 1c. Because of the significant differences in crystal structure between PbSnS_2 and PbS, we can observe definitive (110), (021), and (040) PbSnS_2 reflections irrespective of the PbS reflections. These results suggest that the addition of Sn within PbTe–PbS thermoelectric materials significantly alter the relative solubility of the PbTe and PbS phases. This is interesting in itself since it suggests that small amounts of SnS may be used to control the solubility of PbS and the phase separation process. Only at Sn concentrations larger than 10% is a distinct PbSnS_2 phase observed. Indeed, Sn has been reported as approximately 10% soluble within PbS.²⁸ Our findings suggest that PbSnS_2 is the thermodynamically favorable product between Pb, Te, Sn, and S when the relative concentration between PbS and Sn exceeds 10%. PbSnS_2 (mineralogical name *teallite*)²⁹ is an end member of the SnS mineral series of the orthorhombic space group *Pnma*, GeS structure type. The cell dimensions of PbSnS_2 are $a \times b \times c = 11.17 \times 3.99 \times 4.2$ Å.³⁰ The crystal structures of PbS and PbSnS_2 are somewhat similar:

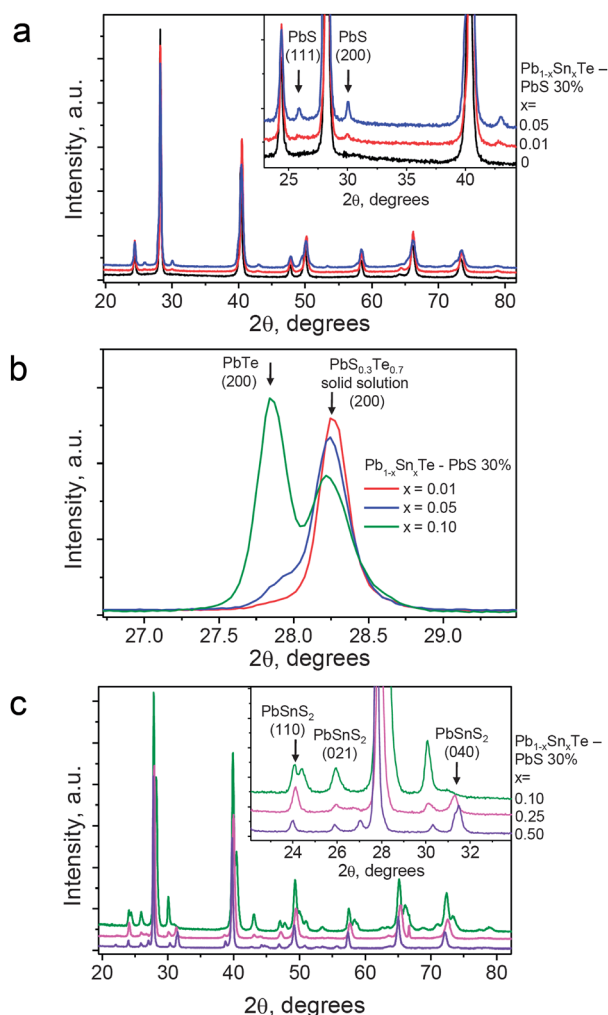


Fig. 1 (a) PXRD of $(\text{Pb}_{1-x}\text{Sn}_x\text{Te})_{0.7}(\text{PbS})_{0.3}$ where $x = 0, 0.01$, and 0.05 . Substitution of even 1% Sn produces significant precipitation of PbS, evidenced by the appearance of PbS (111) and (200) reflections. (b) PXRD of the (200) reflection of PbTe in $(\text{Pb}_{1-x}\text{Sn}_x\text{Te})_{0.7}(\text{PbS})_{0.3}$ where $x = 0.01, 0.05$, and 0.10 , showing the appearance and coexistence of solid solution $\text{PbS}_{1-x}\text{Te}_x$ and PbTe phases. (c) PXRD of $(\text{Pb}_{1-x}\text{Sn}_x\text{Te})_{0.7}(\text{PbS})_{0.3}$ where $x = 0.10, 0.20$, and 0.50 showing appearance of the PbSnS_2 phase, evidenced by (110), (021), and (040) reflections.

the cell dimension of PbS (5.93 \AA) is about half the a axis of PbSnS_2 , and the cube face diagonal $[110]$ (4.19 \AA) corresponds with the a and b axes of PbSnS_2 .²⁶ The crystal structure of PbSnS_2 exhibits Pb–Sn bilayers which form a superstructure along the a axis.³¹

Once we discovered that PbSnS_2 formed as a stable phase within PbTe, we synthesized samples targeting a pseudo-binary mixture of PbTe– PbSnS_2 at compositions up to 33%. The PXRD results of PbTe– PbSnS_2 2, 5, 10, and 20% compositions are shown in Fig. 2a. The PbSnS_2 reflections are clearly observed at concentrations above 10%, under which the phase is undetectable due to limitations in the resolution of the diffractometer. As higher amounts of PbSnS_2 are added to the PbTe matrix, there is also a monotonic shift of the PbTe Bragg peaks to larger 2θ . The corresponding contraction of the PbTe matrix at higher PbSnS_2 concentrations is shown graphically in Fig. 2b. While the PbSnS_2

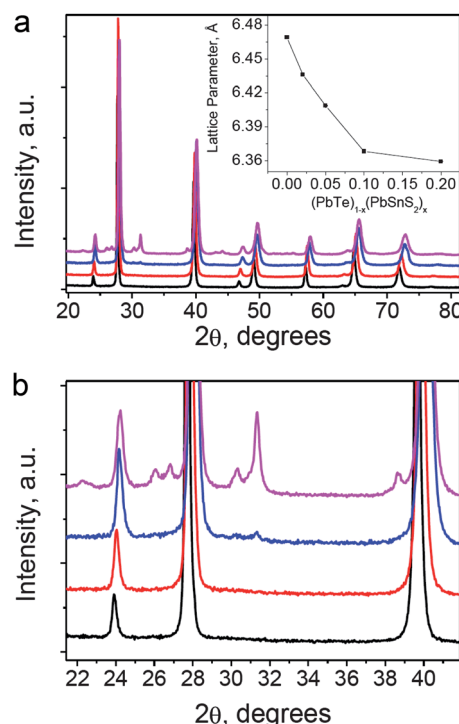


Fig. 2 (a) PXRD of PbTe– PbSnS_2 2, 5, 10, and 20% (bottom to top). The PbSnS_2 phase is clearly observed at concentrations >10%. (b) Detail showing appearance of PbSnS_2 reflections around 26–27 and 30–32 2θ . As increased PbSnS_2 is added, slight substitution of Sn and S within the PbTe results in a monotonic contraction in the lattice, inset of (a).

phase is stable within the PbTe, it is also apparent that some PbSnS_2 is introduced within the PbTe matrix. This conversely suggests increased alloying of Pb and Te within the PbSnS_2 phase, however, at this point it is unclear exactly which atoms are substituting on PbSnS_2 , and at what concentrations.

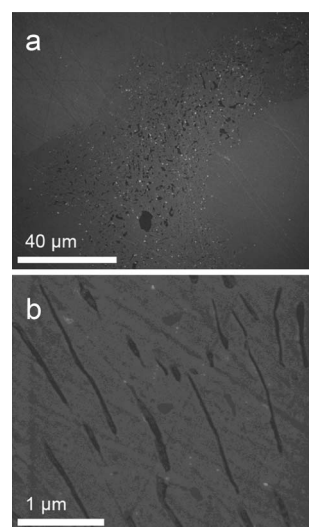


Fig. 3 (a) Low and (b) high magnification SEM images of PbTe– PbSnS_2 6%. The PbSnS_2 phase (dark regions) is formed primarily at the grain boundaries of larger PbTe grains (light regions). The smallest PbSnS_2 regions are 50–100 nm in width, extending microns in length.

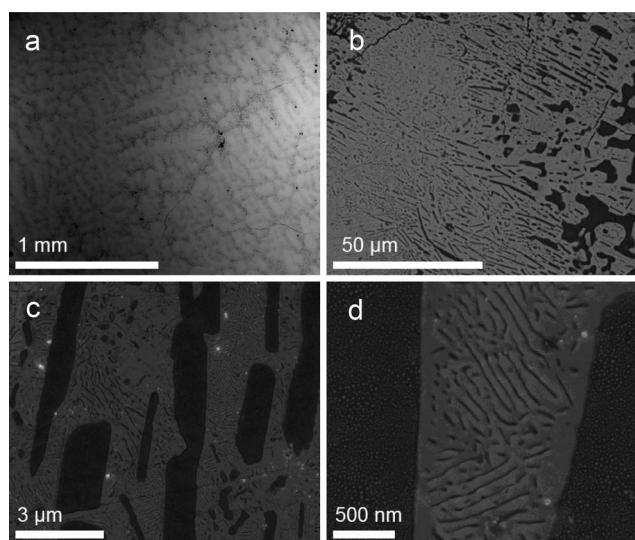


Fig. 4 Microstructure of PbTe–PbSnS₂ 25%. (a) Macro-scale PbSnS₂ networks extending throughout the sample surface, (b) large variation in size distribution between PbSnS₂ particles, (c) and (d) coexistence of large (>1 μm) and small (<100 nm) lamellar structures of PbSnS₂.

Scanning and transmission electron microscopy analysis

To better understand the microstructure and formation chemistry of PbTe–PbSnS₂ materials, we prepared finely polished samples for microstructural analysis using SEM. Because of similarities between the microstructures, we have only included SEM micrographs of the PbTe–PbSnS₂ 6 and 25% compositions in Fig. 3 and 4. The formation of PbSnS₂-rich regions is limited mostly to the grain boundaries of large (>20 μm) grains of PbTe, similar to a eutectic-like formation shown in PbTe–Si/Ge and Sb–Pb composites.^{32–34} At the grain boundaries, the PbSnS₂ phase appears to self-segregate into highly oriented rod-like lamellar structures. There exists a large range of particle sizes, depending on the concentration of PbSnS₂ added. Fig. 3a and b show immiscibility in PbTe–PbSnS₂ 6%.

The largest PbSnS₂ grains are 20–50 μm in size, with a large distribution within the lamellar regions of the PbTe grain boundaries. The highest-density lamellar structures of PbSnS₂ are, on average, approximately 100 nm in width and can extend

for microns in length, Fig. 3b. As higher amounts of PbSnS₂ are added to PbTe, we observe significant precipitation of PbSnS₂. Fig. 4a shows a low magnification SEM micrograph of PbTe–PbSnS₂ 25%. There exists a correlation between PbSnS₂ concentration and PbSnS₂ particle sizes; because of the larger size and dispersity of PbSnS₂ throughout the sample, the interconnected network of PbSnS₂ is clearly observed at the macro-scale in Fig. 4a.

The smallest particles in PbTe–PbSnS₂ 25% appear quite similar in size (~100 nm width, microns in length, Fig. 4a–d) to those observed in PbTe–PbSnS₂ 6% (Fig. 3). However, at concentrations of PbTe–PbSnS₂ >6%, a significant density of large macroscale PbSnS₂ particles were observed, generally between 1 and 10 μm in size, Fig. 4a and b. We show later that these large particles are detrimental to the thermoelectric transport by reducing the electron mobility. For this reason, a balance between the PbSnS₂ particle size and volume density must be achieved to maximize reduced lattice thermal conductivities while not severely limiting electron mobility.

We analyzed the PbTe–PbSnS₂ 11% sample with HRTEM because of the higher volume density of PbSnS₂ particles. The results, shown in Fig. 5, reveal the extended lamellar character of the PbSnS₂ phase and the plate morphology of the embedded crystals. Fig. 5a shows the PbSnS₂ lamellae close to the sample hole. The PbSnS₂ phase appears to self-assemble into rod-like lamellae 50–100 nm in width spaced 100–200 nm apart in the PbTe matrix. Fig. 5b shows electron diffraction patterns with an aperture including the matrix and lamellae along two directions (left [001]_{PbTe} and right [−110]_{PbTe}), which show excellent crystallographic alignment between matrix PbTe and PbSnS₂ lamellae. The atomic-resolution image in Fig. 5c further confirms semi-coherent PbTe–PbSnS₂ interface and also clearly shows the extended superstructure of the Pb–Sn bilayers throughout the lamellae. Fig. 5d is the atomic resolution image of the PbSnS₂ region showed from Fig. 5a and c. There exists a superstructure along the [010] direction, corresponding to the bilayers oriented along the *a* axis in the *Pnma* crystal structure of PbSnS₂, shown in Fig. 5e. Each Pb–Sn bilayer is approximately 0.6 nm in length, agreeing closely with previous PbSnS₂ literature.²⁶ We do not observe a significant volume fraction of small discrete nanostructures (*e.g.* spherical particles <20 nm) in the PbTe–PbSnS₂ system. Previously, we have shown that small nanostructures

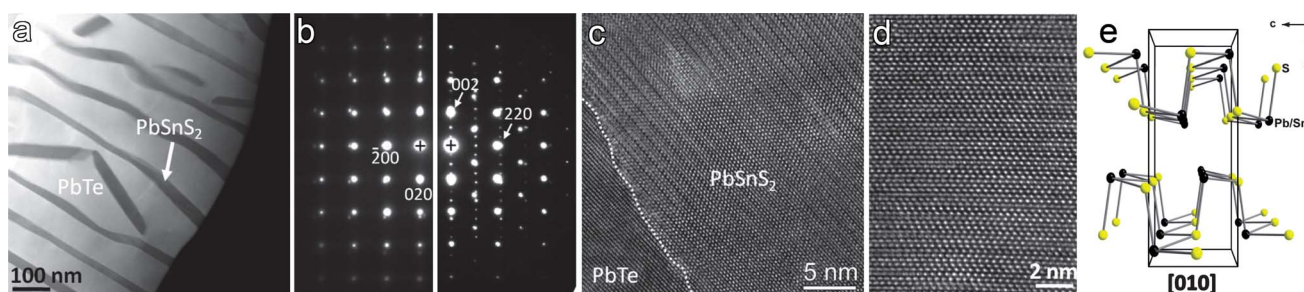


Fig. 5 TEM images of PbTe–PbSnS₂. (a) Low magnification STEM image showing PbSnS₂ lamellae throughout the PbTe matrix, (b) SAED showing characteristic diffraction with the electron beam parallel to [001] (left) and [110] (right) crystallographic planes of PbTe. Along [001], there exists excellent crystallographic alignment between the PbTe matrix and PbSnS₂ lamellae, indicated through the splitting of each diffraction spot dictated by the cubic rocksalt structure of PbTe. Along [010], the superstructure of PbSnS₂ is clearly observed through the periodic satellite reflections not observed in the rocksalt phase. (c) Lattice image along [−110]_{PbTe} direction showing the PbTe–PbSnS₂ interface, (d) enlarged image from (c) showing the natural PbSnS₂ superlattice along [010] the direction. (e) PbSnS₂ crystal structure along [010] for comparison.

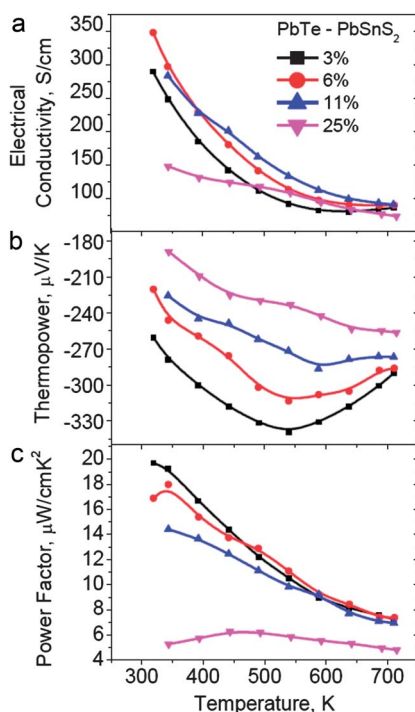


Fig. 6 (a) Electrical conductivity, (b) thermopower, and (c) power factor of undoped PbTe–PbSnS₂ materials.

between 2 and 100 nm in PbTe can reduce the lattice thermal conductivity, such as the embedded spherical and cuboctahedral PbS nanostructures in PbTe–PbS materials.^{24,35} Here, we observed mostly larger rod-like lamellae of PbSnS₂ embedded in PbTe, but the PbSnS₂ regions are naturally nanostructured owing to their unique crystalline structure to produce the Pb–Sn bilayers, shown in Fig. 5d. We believe this observation to be quite important in understanding the low values of lattice thermal conductivity, discussed later.

Thermoelectric properties measurements

The thermoelectric properties of PbTe–PbSnS₂ materials were studied in samples prepared with and without PbI₂ as an n-type dopant. We used 0.055 mol% PbI₂ because this amount has been found to be near optimum to maximize the power factor. The electronic transport properties of undoped (no PbI₂ added) samples of PbTe–PbSnS₂ are shown in Fig. 6a–c. All samples show n-type conduction, low electrical conductivity, and a monotonically increasing thermopower as a function of PbSnS₂ incorporation. The increased thermopower with increased PbSnS₂ concentration is likely an effect both of Sn and S substitution of Pb and Te within the Te matrix, producing concurrent changes to the electron carrier density and mobility, in addition to any modification of the PbTe band structure. The PbTe–PbSnS₂ 3 and 6% samples exhibit optimal properties, with a room temperature power factor of 18–20 μW cm^{−1} K^{−2}, Fig. 6c.

The total thermal conductivity of undoped PbTe–PbSnS₂ composites are shown in Fig. 7a. We observed low values of total thermal conductivity that monotonically decrease with increasing PbSnS₂ incorporation, with values below 1 W m^{−1} K^{−1} over the

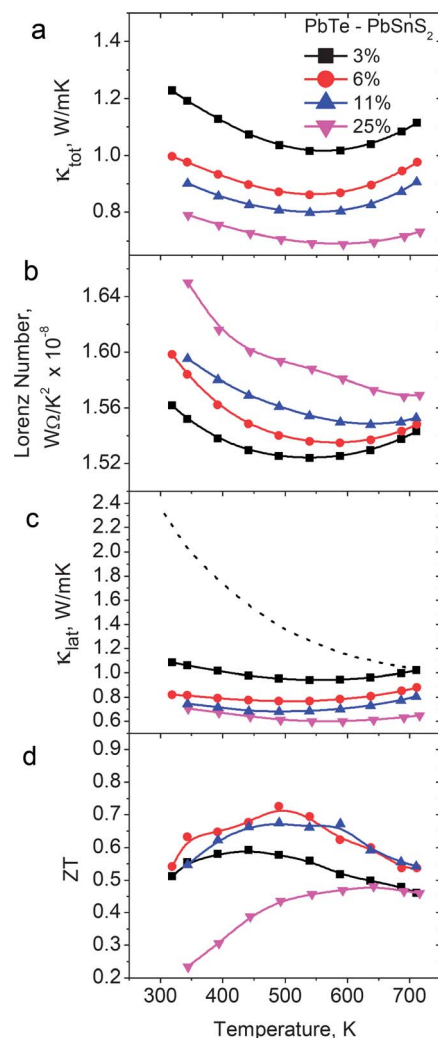


Fig. 7 (a) Total thermal conductivity, (b) calculated Lorenz number, (c) lattice thermal conductivity, and (d) ZT of undoped PbTe–PbSnS₂ materials. In (c), lattice thermal conductivity of pure PbTe is shown by the dashed line.

entire temperature range for composites $\geq 6\%$ PbSnS₂ indicating a lack of charge carriers. To calculate the lattice thermal conductivity, we calculated the Lorenz number from the measured thermopower values as has been described previously.³⁶ The Lorenz values were then used to calculate the electronic contribution to thermal conductivity using the Wiedemann–Franz law, $\kappa_{\text{elec}} = L\sigma T$ (where L = Lorenz number, σ = measured electrical conductivity, and T = temperature). The thermal transport and calculated ZT for undoped PbTe–PbSnS₂ is shown in Fig. 7a–d. The calculated Lorenz numbers shown in Fig. 7b accentuate the need to properly consider the approach toward calculating lattice thermal conductivity.

Because of the low carrier densities within these undoped samples, the calculated Lorenz values are approximately 65% of the Sommerfeld value of 2.45×10^{-8} WΩ/K². Still, the lattice thermal conductivities are extremely low for each sample, between 0.6 and 0.8 W m^{−1} K^{−1} over the entire temperature range for PbTe–PbSnS₂ 6, 11, and 25%, Fig. 7c. As a result, the room temperature ZT of the undoped PbTe–PbSnS₂ 6% sample

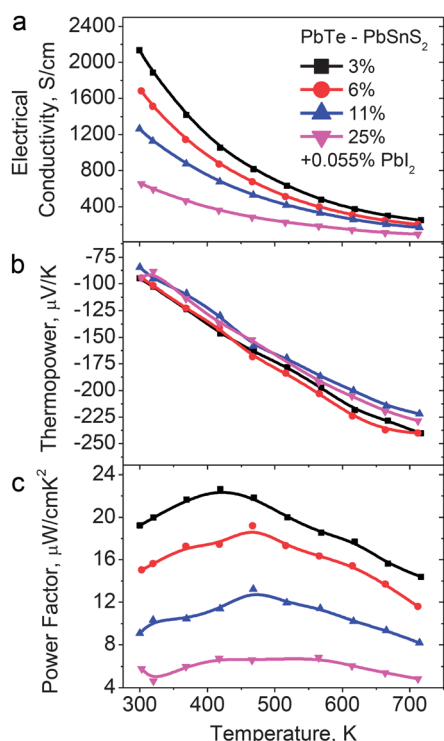


Fig. 8 (a) Electrical conductivity, (b) thermopower, and (c) power factor of 0.055% PbI_2 n-type PbTe-PbSnS_2 materials.

is approximately 0.65, an excellent value for a PbTe -based system, with a maximum of 0.7 at 500 K, Fig. 7d. This sample has the highest room temperature ZT value for a PbTe -based material of 0.55–0.6. The enhancement in ZT appears to be almost exclusively related to the significant reduction in lattice thermal conductivity as compared to pure PbTe . Previously, such effects were seen only in nanostructured thermoelectrics, such as PbTe-PbS .²⁴

Samples of PbTe-PbSnS_2 doped with 0.055% PbI_2 exhibit increased in electrical conductivity Fig. 8a. Across the composition range the thermopower does not change significantly, Fig. 8b, while the electrical conductivity decreases monotonically with increasing PbSnS_2 concentration, varying between $\sim 2200 \text{ S cm}^{-1}$ for PbTe-PbSnS_2 3% to $\sim 600 \text{ S cm}^{-1}$ for PbTe-PbSnS_2 25% at room temperature. The similar values of thermopower regardless of PbSnS_2 fraction suggest similar carrier concentrations for each sample. Because of this, the power factors of the samples steadily decrease with rising PbSnS_2 concentration, each exhibiting a maximum around 450 K.

The thermal transport and ZT of the n-doped PbTe-PbSnS_2 materials are shown in Fig. 9a–d. The total thermal conductivities of the samples, Fig. 9a, show a significant variance between 3 and 6% PbSnS_2 incorporation. A less pronounced difference in total thermal conductivities exist between the PbTe-PbSnS_2 6, 11, and 25% samples; however, the thermal conductivities all three samples at 700 K fall below $1 \text{ W m}^{-1} \text{ K}^{-1}$ and are exceptionally low for heavily doped PbTe . Lorenz numbers and lattice thermal conductivities were calculated in same manner as explained above, Fig. 9b and c. We observe a minimum in lattice thermal conductivity for the PbTe-PbSnS_2 6% sample, with values between 0.5 and $0.75 \text{ W m}^{-1} \text{ K}^{-1}$ over the entire

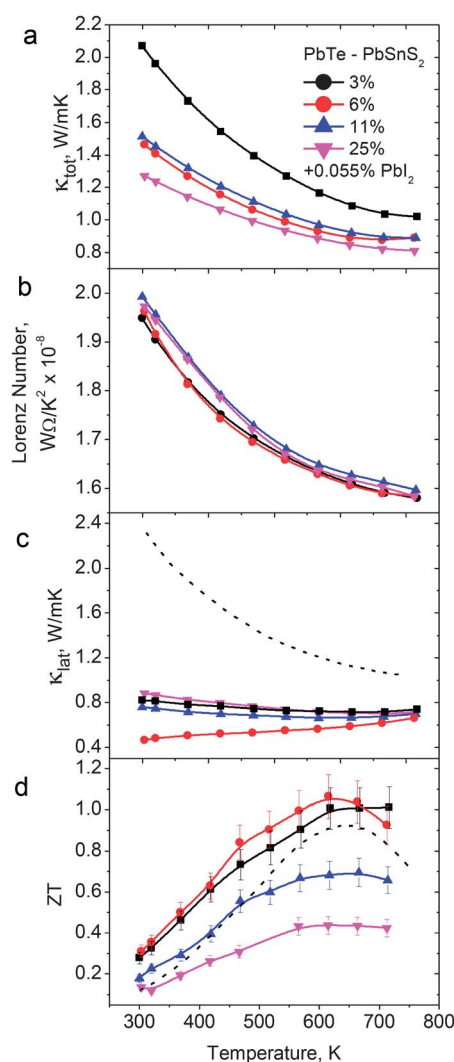


Fig. 9 (a) Total thermal conductivity, (b) calculated Lorenz number, (c) lattice thermal conductivity, and (d) ZT of 0.055% PbI_2 n-type PbTe-PbSnS_2 materials. In (c) and (d), values for pure PbTe is shown by the dashed line. Error bars are included (d) accounting for 10% error associated with the calculation of ZT .

temperature range. Because of the reduced lattice thermal conductivities, especially in the PbTe-PbSnS_2 3 and 6%, we observe an enhancement in ZT over pure PbTe , with a maximum ZT of 1.1 at 625 K, Fig. 9d.

Hall effect measurements

The electron concentration and carrier mobilities were estimated using high-temperature Hall effect measurements. Assuming a single parabolic band, the electron concentration was calculated from the Hall coefficient R_H using the equation $n = 1/eR_H$. The electron mobility was then determined from measured electrical conductivity σ , understanding $\sigma = ne\mu$, where n = carrier concentration, e = fundamental electron charge, and μ = electron mobility. The results are shown in Fig. 10a and b. Increased PbSnS_2 concentration has little effect on the carrier concentration (*i.e.* doping) of the system, which is more heavily affected through added PbI_2 . Indeed, the variance between samples is

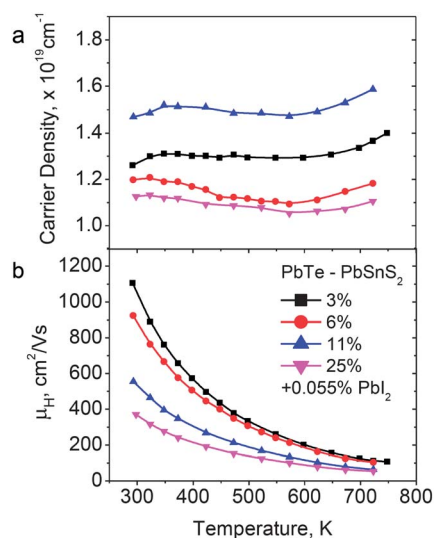


Fig. 10 (a) Electron carrier concentration and (b) electron mobilities of 0.055% PbI₂ n-type PbTe–PbSnS₂ materials.

minimal, between 1.1 and $1.6 \times 10^{19} \text{ cm}^{-3}$. However, the electron mobilities are significantly reduced as PbSnS₂ incorporation increases, Fig. 10b. At room temperature, the mobilities are reduced from $\sim 1100 \text{ cm}^2 \text{ V}^{-1} \text{ s}^{-1}$ for PbTe–PbSnS₂ 3% to $\sim 400 \text{ cm}^2 \text{ V}^{-1} \text{ s}^{-1}$ for PbTe–PbSnS₂ 25%. At temperatures close to 700 K, increased electron scattering decreases the disparity between the samples; however the trend of reduced electron mobility at higher PbSnS₂ concentration is preserved. Therefore, we can conclude from these data that the monotonic decrease in the power factor is almost exclusively a result of enhanced electron scattering upon the addition of higher concentrations of PbSnS₂.

IR reflectivity spectra

The study of the reflectivity, R , as a function of energy in the infrared part of the electromagnetic spectrum yields useful information about basic materials parameters, such as the effective mass, which is directly related to the band masses near the Fermi level. In general, the measurements of the susceptibility effective mass m_s^* using IR reflectivity is based on the fact that R actually reflects the contribution of both the free carriers and the bound electrons to the complex dielectric function $\epsilon(\omega)$.³⁷ Therefore, we have performed room temperature infrared reflectivity measurements of PbTe–PbSnS₂ 3%, 6%, 11% and 25% compositions doped with PbI₂ as an independent, yet direct, method of probing the electron effective mass in order to compare the results with those of transport measurements.

Fig. 11a displays the room temperature IR reflectivity spectra of the studied compositions in the frequency range 100–1500 cm^{-1} . In all cases, the experimental spectra are dominated by free carrier effects, showing high reflectivity values in the low frequency range, accompanied by a deep reflectivity minimum in the range of $\sim 600 \text{ cm}^{-1}$, while for frequencies higher than the minimum the spectra show nearly constant values. The Kramers–Kronig transformation of the experimental reflectivity (see the Experimental section for details) yielded the $\text{Im}(-1/\epsilon)$ spectra

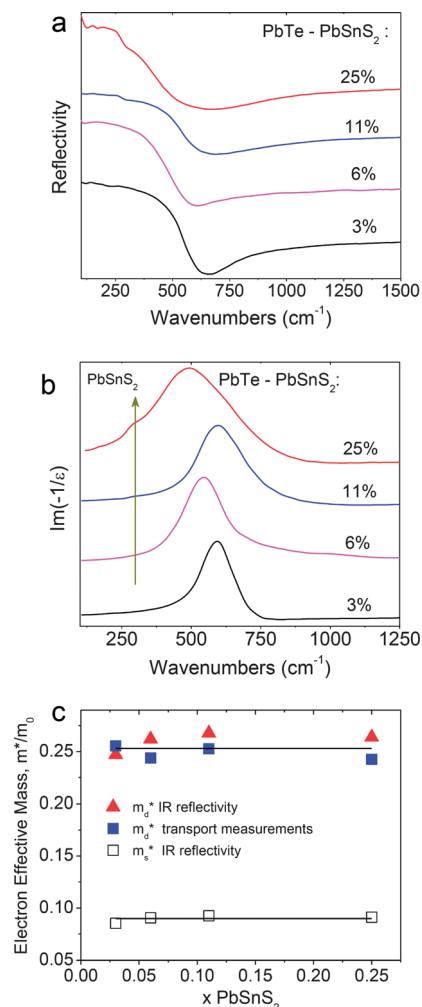


Fig. 11 (a) Experimental reflectivity spectra of the 0.055% PbI₂ doped PbTe–PbSnS₂ compositions. (b) Kramers–Kronig obtained $\text{Im}(-1/\epsilon)$ spectra. The peak frequencies are associated with the free carrier collective oscillations. $R(\omega)$ and $\text{Im}(-1/\epsilon)$ spectra are shifted vertically to each other for ease comparison. (c) The susceptibility effective mass m_s^* (open squares) and the density of states effective mass m_d^* obtained from IR reflectivity (red triangles) and transport measurements (blue squares). Solid lines are guides to the eyes.

displayed in Fig. 11b, peaks of which are associated with the oscillating frequency of the free carriers collective vibrations, ω_p .

As can be seen from Fig. 11b, the plasmon frequency is located in the frequency range ~ 500 to 600 cm^{-1} for all the studied compositions. Two combined effective medium approximations (EMA), as reported elsewhere,³⁸ were adopted for detailed analysis of IR reflectivity data, in order to determine the volume fractions and the dielectric function of the composites. Here we limit our discussion to the effect of PbSnS₂ in plasma frequency and free carrier effective mass.

The plasma frequency is related to the electric susceptibility effective mass, m_s^* , through the relation:

$$\omega_p^2 = \frac{Ne}{\epsilon_0 \epsilon_\infty m_s^*} \quad (2)$$

where N is the carrier concentration, ϵ_0 and ϵ_∞ stand for the vacuum permeability and the high frequency (or optical)

dielectric constant, associated with the contribution of the bound electrons, and e is the electronic charge.³⁷

The values of ω_P are determined from the peak value of the $\text{Im}(-1/\epsilon)$ spectra of Fig. 11b. The composite microstructure of the system affects the high frequency dielectric constant. According to the EMA,³⁷ the ϵ_∞ of a composite material deduced from reflectivity measurements is actually a weighted sum of the ϵ_∞ values of the two constituents of the composite, in our case the PbTe-rich matrix and the PbSnS₂-rich inclusion.³⁹ Based on the IR reflectivity spectra of the undoped $(1-x)\text{PbTe}-x\text{PbSnS}_2$ system with $x = 0.03, 0.06, 0.11$ and 0.33 we concluded that the composition of the matrix is close to $\text{PbTe}_{0.98}\text{S}_{0.02}$.⁴⁰ A high frequency dielectric constant 40 has been obtained for this composition,⁴¹ which is the value of ϵ_∞ we used for our susceptibility effective mass calculations by means of eqn (2).

The calculated susceptibility effective masses, shown as open squares in Fig. 11c, were found almost constant in the whole composition range with values $m_s^*/m_0 \sim 0.09$. Another effective mass, the density of states effective mass m_d^* arises when, for the purpose of statistical computation, the distribution of allowed energy level in the conduction band is replaced by a single level having degeneracy N_m at the band edge.⁴² The density of states effective mass is related to the susceptibility effective mass *via* the relation:

$$m_d^* = N_m^{2/3} \frac{1 + 2K}{3K^{3/2}} m_s^* \quad (3)$$

where N_m is the number of equivalent ellipsoids in the end of Brillouin zone and K is the longitudinal to transverse mass ratio, *i.e.* the mass anisotropy for a given ellipsoid.^{43,44} Using oscillatory magnetoresistance measurements and IR reflectivity studies, Cuff *et al.*⁴⁵ and Lyden⁴² deduced that for n-type PbTe the conduction band consists of four equivalent prolate ellipsoids, $N_m = 4$, while the room temperature mass anisotropy factor was determined $K = 4$.

Using as input values in eqn (3) the N_m and K values from literature^{42,45} and our susceptibility effective mass calculations, we obtained the density of states effective mass m_d^*/m_0 in the whole composition range and the results are shown as red triangles in Fig. 11c. As can be seen from Fig. 11c, the density of states effective mass, following the trend of m_s^*/m_0 , is almost independent from PbSnS₂ concentrations and yields values $m_d^*/m_0 \sim 0.24\text{--}0.26$. In the same Fig. 11c we present the density of states effective mass (full squares) as obtained from the transport measurements of the studied system using the equation:

$$S = \frac{8\pi k_b^2}{3eh^2} m_d^* T \left(\frac{\pi}{3N} \right)^{2/3} \quad (4)$$

where S is the Seebeck coefficient, k_b is the Boltzmann constant, T is the temperature, and N is the carrier concentration.³⁴ As can be seen, the agreement between the optically extracted and the transport extracted m_d^* values is quite good.

The Hall measurements of the PbTe–PbSnS₂ system demonstrated that increased PbSnS₂ concentration has little effect on the carrier concentration (*i.e.* doping) of the system and the variance between samples is minimal, between 1.1 and $1.6 \times 10^{19} \text{ cm}^{-3}$ (see Fig. 10a). Considering the fact that for a specific temperature the effective mass depends on the carrier

concentrations, we feel that the obtained magnitude of the electron effective masses of Fig. 11c is the result of the nearly constant electron concentrations in the studied compositions. This would seem to demonstrate that the energy band structure of the PbTe-rich matrix, giving rise to the effective mass, does not seem to be affected by the introduction of PbSnS₂.

The carrier mobility, μ , is related to the carrier effective mass and the carrier relaxation time, τ , *via* the relation $\mu = e\tau/m^*$,³⁷ meaning that the increase of scattering and/or the increase of the effective mass may lead to the mobility reduction. As shown in Fig. 10b and c, the room temperature mobilities are reduced from $\sim 1100 \text{ cm}^2 \text{ V}^{-1} \text{ s}^{-1}$ for PbTe–PbSnS₂ 3% to $\sim 400 \text{ cm}^2 \text{ V}^{-1} \text{ s}^{-1}$ for PbTe–PbSnS₂ 25%. Based on both the IR and the Hall Effect measurements, the main factor for the room temperature electron mobility reduction is the enhanced electron scattering upon the addition of PbSnS₂.

Conclusions

While the PbTe–SnTe alloy and PbTe–PbS composite systems have been extensively studied, we show here for the first time that the a combination of PbTe, SnTe, and PbS (or any combination thereof) produces a thermodynamically stable pseudo-binary composite of PbTe–PbSnS₂. The PbSnS₂ naturally phase separates from the PbTe matrix on cooling, forming ribbon-like lamellar structures similar to eutectoid solidification. The embedded PbSnS₂ regions within PbTe range between 50 nm to 50 μm in width and can extend microns in length, and appear to form semicoherent interfaces with the PbTe matrix. The crystal structure of the PbSnS₂ lamellae resembles a nanostructured superlattice where each slab is approximately 0.6 nm in thickness that result from the Pb–Sn bilayers of the orthorhombic crystal structure. We find that incorporation of PbSnS₂ in PbTe reduces the lattice thermal conductivity 50–70% over that of PbTe, despite the large size of the PbSnS₂ features (>50 nm). In a corresponding report, we will investigate more fully the source of this low lattice thermal conductivity using detailed TEM and first-principle calculations. Along with the reduction in lattice thermal conductivity, the PbSnS₂ also significantly reduces electron mobilities, as evidenced by Hall effect and IR measurements. Furthermore, calculations of the electron effective mass reveal that the electronic band structure of PbTe is not significantly altered with increasing PbSnS₂ incorporation. We show a ZT of 1.1 for PbI₂-doped PbTe–PbSnS₂ 6%.

What is best: microstructure or nanostructure? At this junction, it would appear that nanostructures have the upper hand. While the microstructured PbTe–PbSnS₂ demonstrates low lattice thermal conductivity, the significantly reduced electron mobility deleteriously dampens the thermoelectric power factor. The small size of nanostructures, in many cases, are immune to this detriment; this is the reason why nanostructured thermoelectrics have demonstrated such low lattice thermal conductivities while also boasting excellent thermoelectric power factor. Since PbSnS₂ is isostructural with a number of metal chalcogenides, namely SnS, SnSe, GeS, GeSe, and their alloys with Pb it is possible that similar materials may be utilized in a number of thermoelectric materials systems to more effectively reduce the thermal conductivity towards producing enhanced ZT . It has been shown previously that larger embedded microstructural

features (*i.e.* >20 nm) in PbTe may reduce lattice thermal conductivity;⁴⁶ here we show a novel PbTe composite system wherein lattice thermal conductivity may be reduced through the incorporations of 'large' but naturally nanostructured features.⁴⁷

Acknowledgements

This material is based upon work supported as part of the Revolutionary Materials for Solid State Energy Conversion, an Energy Frontier Research Center funded by the U.S. Department of Energy, Office of Science, Office of Basic Energy Sciences under Award Number DE-SC0001054. The SEM and TEM work was performed in the EPIC facility of the NUANCE Center at Northwestern University. The NUANCE Center is supported by NSF-NSEC, NSF-MRSEC, Keck Foundation, the State of Illinois, and Northwestern University.

Notes and references

- 1 T. J. Seebeck, *Abh. K. Akad. Wiss. Berlin*, 1821, 289–346.
- 2 A. F. Ioffe, *Semiconductor Thermoelements and Thermoelectric Cooling*, Infosearch, London, 1957.
- 3 L. E. Bell, *Science*, 2008, **321**, 1457–1461.
- 4 C. J. Vineis, A. Shakouri, A. Majumdar and M. G. Kanatzidis, *Adv. Mater.*, 2010, **22**, 3970–3980.
- 5 M. G. Kanatzidis, *Chem. Mater.*, 2009, **22**, 648–659.
- 6 J. R. Sootsman, D. Y. Chung and M. G. Kanatzidis, *Angew. Chem., Int. Ed.*, 2009, **48**, 8616–8639.
- 7 K. F. Hsu, S. Loo, F. Guo, W. Chen, J. S. Dyck, C. Uher, T. Hogan, E. K. Polychroniadis and M. C. Kanatzidis, *Science*, 2004, **303**, 818–821.
- 8 P. F. P. Poudeu, J. D'Angelo, A. D. Downey, J. L. Short, T. P. Hogan and M. G. Kanatzidis, *Angew. Chem., Int. Ed.*, 2006, **45**, 3835–3839.
- 9 R. Venkatasubramanian, *Phys. Rev. B: Condens. Matter Mater. Phys.*, 2000, **61**, 3091.
- 10 A. I. Hochbaum, R. Chen, R. D. Delgado, W. Liang, E. C. Garnett, M. Najarian, A. Majumdar and P. Yang, *Nature*, 2008, **451**, 163–167.
- 11 W. Kim, J. Zide, A. Gossard, D. Klenov, S. Stemmer, A. Shakouri and A. Majumdar, *Phys. Rev. Lett.*, 2006, **96**, 045901.
- 12 J. M. Higgins, A. L. Schmitt, I. A. Guzei and S. Jin, *J. Am. Chem. Soc.*, 2008, **130**, 16086–16094.
- 13 Y. Lan, A. J. Minnich, G. Chen and Z. Ren, *Adv. Funct. Mater.*, 2010, **20**, 357–376.
- 14 B. Poudel, Q. Hao, Y. Ma, Y. Lan, A. Minnich, B. Yu, X. Yan, D. Wang, A. Muto, D. Vashaee, X. Chen, J. Liu, M. S. Dresselhaus, G. Chen and Z. Ren, *Science*, 2008, **320**, 634–638.
- 15 W. Xie, J. He, H. J. Kang, X. Tang, S. Zhu, M. Laver, S. Wang, J. R. D. Copley, C. M. Brown, Q. Zhang and T. M. Tritt, *Nano Lett.*, 2010, **10**, 3283–3289.
- 16 P. N. Alboni, X. Ji, J. He, N. Gothard and T. M. Tritt, *J. Appl. Phys.*, 2008, **103**, 113707.
- 17 Y. Zhang, H. Wang, S. Kräemer, Y. Shi, F. Zhang, M. Snedaker, K. Ding, M. Moskovits, G. J. Snyder and G. D. Stucky, *ACS Nano*, 2011, **5**, 3158–3165.
- 18 G. J. Snyder and E. S. Toberer, *Nat. Mater.*, 2008, **7**, 105–114.
- 19 K. Biswas, J. He, Q. Zhang, G. Wang, C. Uher, V. P. Dravid and M. G. Kanatzidis, *Nat. Chem.*, 2011, **3**, 160–166.
- 20 K. Biswas, J. He, G. Wang, S.-H. Lo, C. Uher, V. P. Dravid and M. G. Kanatzidis, *Energy Environ. Sci.*, 2011, **4**, 4675–4684.
- 21 A. Shakouri and M. Zebbarj, *Nanoengineered Materials for Thermoelectric Energy Conversion: Thermal Nanosystems and Nanomaterials*, ed. S. Volz, Springer, Berlin/Heidelberg, 2009, vol. 118, pp. 225–299.
- 22 J. Androulakis, C.-H. Lin, H.-J. Kong, C. Uher, C.-I. Wu, T. Hogan, B. A. Cook, T. Caillat, K. M. Paraskevopoulos and M. G. Kanatzidis, *J. Am. Chem. Soc.*, 2007, **129**, 9780–9788.
- 23 J. He, S. N. Girard, M. G. Kanatzidis and V. P. Dravid, *Adv. Funct. Mater.*, 2010, **20**, 764–772.
- 24 S. N. Girard, J. He, C. Li, S. Moses, G. Wang, C. Uher, V. P. Dravid and M. G. Kanatzidis, *Nano Lett.*, 2010, **10**, 2825–2831.
- 25 M. Orihashi, Y. Noda, L. D. Chen, T. Goto and T. Hirai, *J. Phys. Chem. Solids*, 2000, **61**, 919–923.
- 26 L. L. Y. Chang and W. R. Brice, *Mineral. Mag.*, 1971, **38**, 186–189.
- 27 L. Solymar and D. Walsh, *Electrical Properties of Materials*, Oxford Press, 2004.
- 28 V. G. Kuznetsov and L. Ch'ih-fa, *Russ. J. Inorg. Chem.*, 1964, **9**, 656–659.
- 29 G. T. Prior, *Z. Kristallogr. Mineral.*, 1904, 21–27.
- 30 K. Hayashi, A. Kitakaze and A. Sugaki, *Mineral. Mag.*, 2001, **65**, 645–651.
- 31 I. V. Slipukhina and D. M. Bercha, *Phys. Status Solidi B*, 2007, **244**, 650–668.
- 32 J. R. Sootsman, J. He, V. P. Dravid, S. Ballikaya, D. Vermeulen, C. Uher and M. G. Kanatzidis, *Chem. Mater.*, 2009, **22**, 869–875.
- 33 J. R. Sootsman, H. Kong, C. Uher, J. J. D'Angelo, C. I. Wu, T. P. Hogan, T. Caillat and M. G. Kanatzidis, *Angew. Chem., Int. Ed.*, 2008, **47**, 8618–8622.
- 34 J. R. Sootsman, J. He, V. P. Dravid, C.-P. Li, C. Uher and M. G. Kanatzidis, *J. Appl. Phys.*, 2009, **105**, 083718.
- 35 S. N. Girard, J. He, X. Zhou, D. Shoemaker, C. M. Jaworski, C. Uher, V. P. Dravid, J. P. Heremans and M. G. Kanatzidis, *J. Am. Chem. Soc.*, 2011, **133**, 16588–16597.
- 36 S. Johnsen, J. He, J. Androulakis, V. P. Dravid, I. Todorov, D. Y. Chung and M. G. Kanatzidis, *J. Am. Chem. Soc.*, 2011, **133**, 3460–3470.
- 37 J. R. Dixon and H. R. Riedl, *Phys. Rev.*, 1965, **138**, A873.
- 38 T. C. Hasapis, S. N. Girard, E. Hatzikraniotis, K. M. Paraskevopoulos and M. G. Kanatzidis, *J. Nano Res.*, 2012, **17**, 165.
- 39 D. Stroud and F. P. Pan, *Phys. Rev. B: Solid State*, 1978, **17**, 1602–1610.
- 40 T. C. Hasapis, S. N. Girard, E. Hatzikraniotis, K. M. Paraskevopoulos and M. G. Kanatzidis, *Mater. Res. Soc. Symp. Proc.*, 2011, **1325**, 143.
- 41 J. M. Miljković, N. Romčević, Z. V. Popovic, W. Köning and V. N. Nikiforov, *Phys. Status Solidi B*, 1996, **193**, 43–51.
- 42 H. A. Lyden, *Phys. Rev.*, 1964, **135**, A514–A521.
- 43 W. Zawadzki, *Adv. Phys.*, 1974, **23**, 435–522.
- 44 A. Aziza, E. Amzallag and M. Balkanski, *Solid State Commun.*, 1970, **8**, 873–877.
- 45 K. F. Cuff, M. R. Ellett and C. D. Kuglin, *J. Appl. Phys.*, 1961, **32**, 2179–2185.
- 46 Y. Pei, J. Lensch-Falk, E. S. Toberer, D. L. Medlin and G. J. Snyder, *Adv. Funct. Mater.*, 2011, **21**, 241–249.
- 47 J. Q. He, S. N. Girard, J.-C. Zheng, L. D. Zhao, M. G. Kanatzidis and V. P. Dravid, *Adv. Mater.*, 2012, DOI: 10.1002/adma.20121565.